TRAJECTORY DESIGN FOR ASTEROID SAMPLE RETURN COMBINING BALLISTIC CAPTURE AND AEROBRAKING

Zongfu Luo[1], Yijun Lian[2], Chen Zhang[3] & Tao Zhang[1]

[1]School of Systems Science and Engineering, Sun Yat-sen University, 510275 Guangzhou, P. R. China
[2]College of Aerospace Science and Engineering, National University of Defense Technology, 410073 Changsha, P. R. China
[3]Technology and Engineering Center for Space Utilization, Chinese Academy of Sciences, 100094 Beijing, P. R. China

Abstract

A systematic method of constructing low-thrust, low-energy transfers from a near-Earth asteroid to low-Earth orbit with a required inclination is presented, providing an alternative for asteroid sample return scenarios. The rough opportunities of the asteroid departure and the Earth capture are estimated by using the Lambert algorithm, i.e., two-body transfers from the asteroid to the L_1 or L_2 Lagrangian points of the Sun-Earth system. Ballistic capture orbits are generated by manipulating the stable and unstable sets when attractions of the Sun, the Earth, and the Moon are considered. These solutions that can be connected to the asteroid with low-thrust transfers are selected as candidates of the aero-ballistic capture, which utilizes both multi-body dynamics and aerodynamics. An initial perigee maneuver is performed to reduce the post-capture apogee distance and thereafter, a series of apogee trim maneuvers are introduced to maintain the maximum dynamic pressure of each atmospheric passage. Two inclination managing strategies, namely, active control and passive control, respectively, are used. The former uses chemical impulses to correct the inclination discrepancy, and the latter gradually changes it by yawed solar panels. Analytical prediction of the semi-major axis and inclination with respect to the Earth is derived. An time-optimal yawing angle is formulated for the passive control mode. Numerical simulations for the transfer from the asteroid 1991 VG to the International Space Station are implemented.

Keywords: Ballistic capture, Aerobraking, Asteroid Sample Return

1. Introduction

Near-Earth asteroids (NEAs) are asteroids that will closely approach the Earth or cross the Earth's orbit. These objects are of particular interest due to: 1) they may deposit the pristine materials since the early days of our solar system and may be responsible for the origin of life on the Earth; 2) they bear careful monitoring due to their risks of impact with the Earth, e.g., the 99942 Apophis; 3) they contain a variety of valuable materials and substances for industrial and commercial use [1, 2, 3]. Hundreds and thousands of NEAs have been discovered and many more are being anticipated by continuous observations.

Sampling return from the NEAs will give us an in-depth understanding of their structures and compositions [4, 5]. Several asteroid sample return plans have been actualized or proposed recently, as JAXA's Hayabusa 1 and 2 kawaguchi2006, tsuda2013, NASA's OSIRIS-REx [6], and ESA's MarcoPolo-R [7]. These missions will also provide detailed information of NEAs for NASA's Asteroid Redirect Mission (ARM), which plans to identify, capture, and redirect an entire NEA to the Earth-Moon system for scientific investigation and evaluation [8]. In order to enumerate potentially accessible NEAs, scientists have characterized those suitable for future space missions and established a list of "NHATS".[1] Among them, a catalogue of easily retrievable asteroids is provided by using patched conic approximations and low-energy transfers [9, 10, 11, 12, 13, 14].

[1]NHATS: Near-Earth Object Human Space Flight Accessible Targets Study, see http://neo.jpl.nasa.gov/nhats/ [retrieved 12 January 2015].

Without sacrificing the generality, take the successful asteroid sample return mission Hayabusa 1 as an example. The spacecraft was equipped with xenon ion engines and bi-propellant thrusters, whereas the ion engines were used in the cruising phase due to its high specific impulse and the bi-propellant thrusters are prepared for orbital maneuvers (e.g., trajectory correction maneuvers). The re-entry capsule was separated from the main probe three hours before re-entering the Earth's atmosphere. A heavy thermal protection system was designed to protect the capsule from experienced peak deceleration and heating rates [15]. Instead of directly returning to the ground, an alternative option is to inject the spacecraft into low-Earth orbit (LEO) and then to rendezvous with, for instance, the International Space Station (ISS) or to release the re-entry capsule into the Earth's atmosphere with a comparatively lower velocity [8].

Ballistic capture, also known as gravitational capture, can provide a lower re-entry velocity by judicious use of the multi-body dynamics in comparison with that of a classical Hohmann transfer under identical conditions [16, 17, 18, 19, 20, 21]. However, ballistic capture transfer requires longer flight time and its post-capture leg is chaotic and weakly stable, which requires further decelerations to stabilize it [22]. Aerobraking has been proved as an effective strategy to brake the spacecraft when concerning a planet covered with usable atmosphere, although a braking maneuver is, in general, performed to insert the spacecraft into an elliptic-type orbit before aerobraking, e.g., $\Delta v = 973$ m/s for the Mars Global Surveyor mission [23, 24, 25, 26, 27, 28]. The effort of this paper is to combine the advantages of both ballistic capture and aerobraking techniques and, hence, to construct a novel transfer with lower fuel consumption, flexible arriving period, and moderate flight time for asteroid sample returns.

easily retrievable objects (EROs) [29, 30, 31, 32, 33]

The sampling return scenario is scheduled as follows. The spacecraft has a “box-wing” configuration. It departs from the asteroid after finishing proximal operations. Low-thrust engines with a high specific impulse drive the spacecraft to the neighbourhood of the Earth-Moon system (solar sail propulsion is also considered for sample return missions, whereas it is beyond the scope of this paper; see, e.g., [34, 35]). This interplanetary transfer is viewed as a perturbed two-body problem, and subsequently, is patched with a ballistic capture leg before arriving a given periapsis distance, labelled as pre-capture phase. A small periapsis maneuver is performed to arrive a stabler and lower post-capture orbit, where the conventional aerobraking begins. A series of aerobraking trim maneuvers (ABMs) will be performed at apoapsis as necessary to maintain the maximum dynamic pressure of each atmospheric passage. Two strategies, i.e., chemical impulses and yawing angle, are imposed to manage the orbital inclination with respect to the Earth. This parameter is important for the sample's recovery.

The reminder of this paper is arranged as follows. Section 2.provides background notions, including reference frames and dynamical models involved. In Sect. **??**, the basic construction procedure is described which allows us to snap a general understanding of the method proposed. Detailed discussions about ballistic capture and aerobraking are presented in Sect. **??** and **??**. Study case is provided in Sect. 4. Some underlying remarks are drawn in Sect. 5. Two appendixes are reported where analytical derivations are given.

2. Mathematical models

The spacecraft experiences a variety of dynamical environments. The Sun's gravity and low-thrust are functioned on the spacecraft after its departure from the asteroid and before the ballistic capture near the Earth. A critical point, denoted by P, is chosen as the switch of the heliocentric and planetocentric motions. Starting from P, the attractions from the Earth and the Moon are taken into account. The aerodynamic drag is further considered when the spacecraft passes the sensible atmosphere.

Table 1 reports physical and orbital parameters of the celestial bodies involved, i.e., the Sun, the Earth and its satellite Moon. The “primary”, of mass m_p, is the body revolved by the “secondary” of mass m_t, and μ is defined by $\mu = m_t/(m_t + m_p)$. SOI, sphere-of-influence, is defined by $a_t\,(m_t/m_p)^{\frac{2}{5}}$, where a_t is the semi-major axis of the orbit of the secondary relative to its primary. Hill sphere is in concordance with the distances between the secondary and the Lagrangian points L_1 and L_2 in the circular restricted three-body problem (CRTBP); see [36] for details. Both the SOI and Hill sphere is provided in units of the Earth's radius R_e for comparison.

Table 1 – Approximate parameters of the bodies considered in the dynamical model.

Body	Gravity par. km^3/s^2	Radius R, km	Primary	Mass ratio μ	Ecce. e_t	Semi-major axis a_t, $\times R_e$	SOI R_s $\times R_e$	Hill sphere R_h, $\times R_e$
Earth	3.986E+05	6,371.0	Sun	3.003E-06	0.0167	23,466	145.03	235.18
Moon	4.903E+03	1,737.4	Earth	1.215E-02	0.0549	60.33	10.36	9.65

2.1 Reference frames

As the spacecraft in the aforementioned return scenario suffers various dynamical environments, an inertial frame, labelled as (x_i, y_i, z_i), is used to describe the motions for simplicity. In order to control the post-capture orbital parameters and to facilitate the computation, the x_i and y_i axes are defined in the body's mean equator plane at a reference epoch t_0 (the body is referred as the Earth, where the frame is, in general, centered) [22]. The frame is abbreviated to BME@t_0, and its z_i-axis is aligned with the spin axis.

The aerodynamic force functioned on the solar panels is described in a spacecraft central Velocity-Co-normal-Normal frame (VCN), denoted by (x_v, y_v, z_v), as shown in Figure.1. The x_v-axis aligns with its inertial velocity $\boldsymbol{v}$, the y_v-axis goes along the negative orbital normal, and the y_v-axis completes the right-hand triad. The transformation from VCN to BME@t_0 is calculated from

$$\mathcal{Q}_{v\to i}(t_0) = [(\boldsymbol{x}_v)_i \quad (\boldsymbol{y}_v)_i \quad (\boldsymbol{z}_v)_i], \tag{1}$$

and the components in (1) are defined by

$$(\boldsymbol{x}_v)_i = \frac{\boldsymbol{v}}{\|\boldsymbol{v}\|}, \qquad (\boldsymbol{y}_v)_i = \frac{\boldsymbol{v}\times\boldsymbol{r}}{\|\boldsymbol{v}\times\boldsymbol{r}\|}, \qquad (\boldsymbol{z}_v)_i = (\boldsymbol{x}_v)_i \times (\boldsymbol{y}_v)_i, \tag{2}$$

where $\boldsymbol{r}$ and $\boldsymbol{v}$ are the position and velocity vectors with respect to the BME@t_0 frame.

The rotational angle about z_v-axis is called the yaw angle, as shown in Figure.1, which is able to provide aerodynamical forces in two directions, i.e., $\boldsymbol{F}_a^{\perp}$ perpendicular to the orbital plane and $\boldsymbol{F}_a^{\parallel}$ parallel to it. It should be of special note that this is only possible in rarefied gas flow at a relatively high altitude of the atmosphere [15].

2.2 Equations of motion

The governing equations with respect to the BME@t_0 frame are written in the form

$$\begin{aligned} \dot{\boldsymbol{r}} &= \boldsymbol{v} \\ \dot{\boldsymbol{v}} &= \boldsymbol{a}_g + \boldsymbol{a}_t + \boldsymbol{a}_a \\ \dot{m} &= -T/c, \end{aligned} \tag{3}$$

where the terms $\boldsymbol{a}_g$, $\boldsymbol{a}_a$, and $\boldsymbol{a}_t$ are accelerations due to the gravity, the aerodynamic drag, and the low thrust, m is the spacecraft's mass, T is its thrust magnitude, and $c = I_{\text{sp}} g_0$ denotes the exhaust velocity (I_{sp} is the specific impulse of the thrust engine and g_0 is the gravitational acceleration at the sea level). It is also recognized that not all the three accelerations appear for each phase; e.g., $\boldsymbol{a}_g$ and $\boldsymbol{a}_t$ are active before arriving at the switch point P, the low-thrust engines are not activated during the aerobraking, and $\boldsymbol{a}_a$ is only available in proximity of each periapsis.

More precisely, the gravitational acceleration is of the form

$$\boldsymbol{a}_g = -\mu_c \frac{\boldsymbol{r}}{r^3} - \sum_{i\in\mathbb{P}} \mu_i \left(\frac{\boldsymbol{r}_i}{r_i^3} + \frac{\boldsymbol{r}-\boldsymbol{r}_i}{\|\boldsymbol{r}-\boldsymbol{r}_i\|^3} \right), \tag{4}$$

where $\mathbb{P}$ is a set of perturbing bodies. It is empty before arriving the point P, during which the BME@t_0 frame is centered at the Sun and μ_c represents the Sun's gravity parameter. From P onward, the

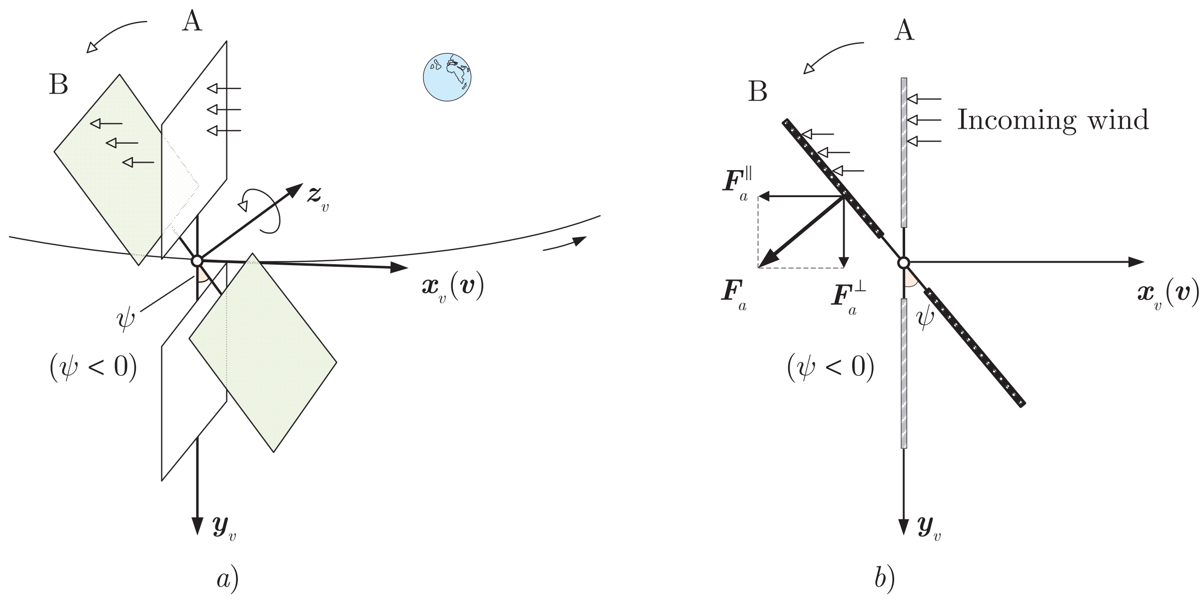

Figure 1 – Yaw angle (ψ) and the aerodynamical force ($\boldsymbol{F}_a$): a) 3-D geometry of the yaw angle; b) Side-view of the panels and aerodynamical force decomposition.

origin of BME@t_0 is switched to the Earth, and hence, μ_c denotes the Earth's gravity parameter. The attractions from the Sun and the Moon are considered by the sum term in Eq. (4). The terms μ_i ($i \in \mathbb{P}$) are their gravitational constants, and r_i are the positions of the spacecraft with respect to them, respectively.
The propulsive acceleration $\boldsymbol{a}_t$ is computed from $\boldsymbol{a}_t = -\boldsymbol{T}/m$, where $\boldsymbol{T}$ is the thrust vector. The onboard engines provide low thrust ($T < 1$ N) with high I_{sp} ($\simeq 3000$ s). The low-thrust technology can greatly expand interplanetary mission capabilities [10, 37, 5].
The aerodynamic acceleration $\boldsymbol{a}_a$ is mostly induced by the solar panels for the "box-wing" architecture. Figure.2 provides four symmetric configurations, where ψ represents the sweep angle of the solar wings from a reference plane and θ is a yawing angle that describes the rotation of the spacecraft along the y_v-axis (e.g., by means of reaction-wheels; see [38]). A positive θ corresponds to a counter-clockwise rotation from the x_v-axis, and conversely, a clockwise rotation means a negative θ. It is observed from Figure.2 that the drags on the "left" and "right" wings are equal for cases (a) to (c), but are unequal for case (d) due to different approaching angles with respect to both wings. Therefore, the angular momentum of both wings are neutralized excepting that of case (d). Only the configurations (a) and (c) are considered in this paper, i.e., $\psi = 0$. Thus, the total drag is always perpendicular to the solar panels. In practice, the wind-relative velocity $\boldsymbol{v}_r$ is not in consistence with $\boldsymbol{v}$ due to the rotating atmosphere (see the angle α in Figure.**??**). Generally, the discrepancy between θ and α is small since the atmospheric rotating velocity is far less than the spacecraft's velocity.

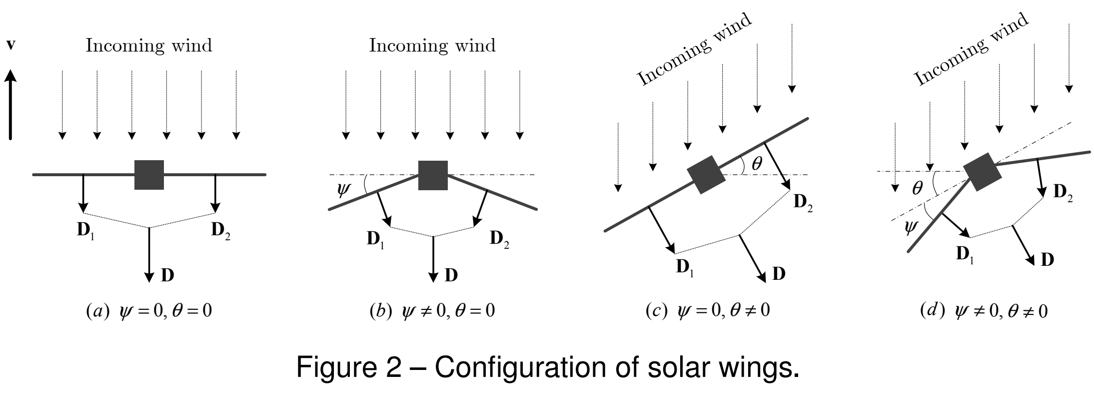

Figure 2 – Configuration of solar wings.

The magnitude of the aerodynamic acceleration is derived from $a_a = \bar{q} C_d S/m$, where $\bar{q} = \rho {v_r}^2/2$ is the dynamic pressure, ρ is the current density at an altitude h, C_d is the spacecraft's drag coefficient, and

S is its reference area. An exponential model is used; i.e., $\rho = \rho_0 \exp -\frac{h-h_0}{H}$, where ρ_0 is a reference density at an altitude of h_0 and H is the corresponding scale height. We assume the drag coefficient is C_{d0} when $\alpha = 0$. Thus, $C_d = C_{d0}\cos^2\alpha$ according to the Newton's sine-squared law in the hypersonic aerodynamics [15]. Apparently, the drag coefficient descends down rapidly with the increase of α. No lift effects are considered. Hence, the aerodynamic acceleration with respect to the BME@t_0 frame is obtained by

$$\boldsymbol{a}_a = a_a \mathscr{Q}_{v\to b}(t_0)\mathscr{R}_y(-\boldsymbol{\theta})\begin{bmatrix}-1\\0\\0\end{bmatrix}, \tag{5}$$

where $\mathscr{R}_y$ is the direction cosine matrix around the y_v-axis.
To avoid precision lost and to accelerate the integrations, the equations of motion (3) are normalized by the parameters in Table 2 for both the interplanetary transfer and the ballistic capture. A 7th/8th order Runge–Kutta–Felhberg method with automatic step-size control is used. The absolute and relative tolerances are both set to 10^{-12}.

Table 2 – Normalization parameters.

Symbol	Remark	Comment	Value	Unit
MU	Gravity parameter unit	Earth's gravity parameter	3.986E+05	km^3/s^2
LU	Length unit	Earth's mean radius	6,371.0	km
TU	Time unit	$\sqrt{\left(LU^3/MU\right)}$	805.46	s
VU	Velocity unit	LU/TU	7.91	km/s
MAU	Mass unit	Reference mass	1,000	kg

3. Methodology

3.1 General framework

As stated in the introduction, the 3D overall trajectory connects an asteroid of interest to a LEO with specified inclination and altitude. Fuel expenditure, other than the flight time, is the primary concern of the mission design. Two critical points along the route, denoted by P_p and $P_{i.c.}$ (as shown in Figure.3), respectively, play key roles in constructing the entire trajectory.

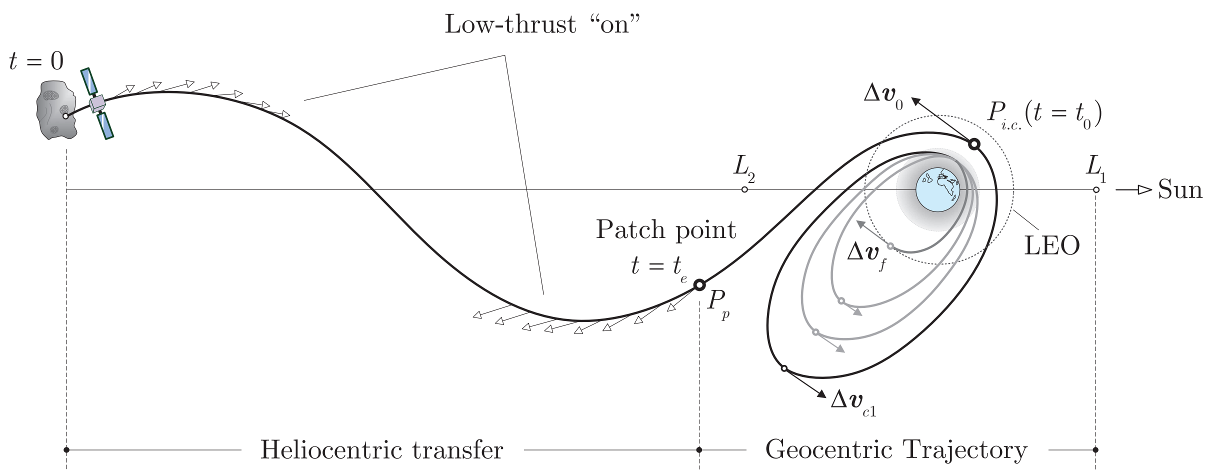

Figure 3 – Overall asteroid sample return trajectory.

The first critical point, P_p, is the patch point that connects the heliocentric transfer arc and the geocentric part. Prior to P_p, only the Sun's gravity is considered for the propagation of the spacecraft's state, while thereafter, the gravities of the Earth, Moon, and Sun will all be taken into account. In other words, P_p is the delimiter of using two-body dynamics or multi-body dynamics. For the two-body part,

in order to minimize the energy cost, optimised low-thrust is to be implemented for the interplanetary heliocentric transfer, which takes as initial guess the Lambert's arcs in an iterative manner, as will be elaborated in Sec.3.2 For the multi-body part, starting from the patch point P_p, impulsive delta-v's are used to construct the ballistic capture trajectory. From a backwards-in-time perspective, P_p can also be viewed as an "escape point".
The second critical point, $P_{i.c.}$, is located at the periapsis of the Earth (see Figure.3) and functions in two aspects. The time epoch associated to $P_{i.c.}$ is denoted by t_0. The first role it plays is to generate the initial conditions for ballistic captures about Earth. This is done by extensive search via numerical integration over a multi-dimensional phase space formed by four classical orbit elements (details given in Sec.3.2 It should be noted that P_p is the end point of the ballistic capture trajectory if propagating P_{IC} backwards in time. The second role $P_{i.c.}$ plays is to initialize the aerobraking process. A delta-v, denoted by $\Delta \boldsymbol{v}_0$, is implemented at $P_{i.c.}$ in order to shorten the range that the trajectory thereafter can reach and, meanwhile, to redirect the spacecraft to a certain level of atmosphere. The detailed aerobraking process is given in Sec.3.3

3.2 Phase I: Patching interplanetary transfer and ballistic capture

The objective of this design phase is to obtain a transfer trajectory that connects the departure point on the asteroid and the arrival point at the periapsis of the Earth, i.e., $P_{i.c.}$. The entire trajectory is in fact composed of two segments that are patched at P_p. Four major steps are taken to accomplish the task.

3.2.1 Step 1: Patch time estimation

The journey from the asteroid to the vicinity of the Earth accounts for the major part of both the time and the fuel expenditure, and therefore should be handled in the first place. Without loosing generality, we assume the departure time from the asteroid is $t = 0$.
Since the patch point P_p is still undetermined at this step, the idea is to use the Sun-Earth L_1/L_2 as destinations to estimate the time and energy cost, as shown in Figure.4. It is because, as revealed in [39, 40], the Jacobi integral of the spacecraft following a ballistic capture transfer to the vicinity of L_1 or L_2 is approximately equal to the Jacobi integral of L_1 or L_2, respectively. This fact would help to insure a smooth transition to the ballistic capture part starting from P_p.

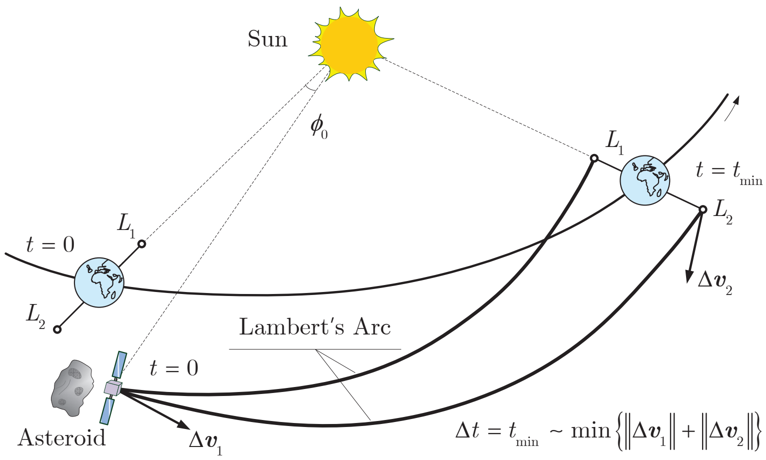

Figure 4 – Time and energy cost estimation by using Lambert arcs.

As stated above, only the Sun's gravity is considered during the heliocentric transfer part, so impulsive Lambert arc can be readily computed from a given departure date and a time of flight (TOF). The total delta-v is the sum of the two ones at both ends, denoted by $\Delta \boldsymbol{v}_1$ and $\Delta \boldsymbol{v}_2$, respectively, as shown in Figure.4. An extensive search over different combinations of the departure date and TOF is implemented respectively for L_1 and L_2, since the objective of this step is to find among innumerous candidates the best Lambert arc with the minimum total delta-v, as well as the associated TOF (the same as the final time epoch) denoted by t_{min}. As will be shown in the following, t_{min} will be used as a good reference for the further refinement of the patch time.

3.2.2 Step 2: Ballistic capture construction

Now the focus is directed to the first periapsis of the Earth ($P_{i.c.}$ in Figure.3), where the construction of the ballistic capture trajectory is initialized by following the procedure preliminaryly described in hyeraci2010 and later generalized in luo2014a. For the completeness of the work, it is briefly outlined as follows.

In the first place, the spacecraft state at $P_{i.c.}$ ($t = t_0$) can be computed from the initial condition (i.c.) defined by the classical orbit elements in the BME@t_0 frame. Combining the sampling of each element within its valid range will generate a large population of i.c.'s. Note that the orbit inclination i_0 has been specified for a given mission, and the true anomaly f_0 always equals zero because $P_{i.c.}$ is located at the periapsis.

Each i.c. of the spacecraft is propagated by both forward and backward integration using Eq. (3). We note that t_0 plays an essential role in constructing the capture orbit because it correlates with different relative configurations of the Moon, the Earth and the Sun, whose gravities are all considered in the numerical integration. Based on t_{min}, the value of t_0 is taken from a discretized time span, therefore adding one more dimension to the problem of ballistic capture orbit design. According to the follow-on behaviors in both directions, the i.c.'s are classified into different sets [22, 31]. The related two ones are:

1) Weakly Stable Set, $\mathscr{W}_n$ ($n \geq 1$): whose orbits perform n complete revolutions about the Earth without impacting with or escaping from it when integrating forward in time;

2) Unstable Set, $\mathscr{X}_{-1}$: whose orbits escape from the Earth without completing any revolution around or impacting with it when integrating backward in time.

For the backwards integration leg, we introduce an escape criterion, which judges the spacecraft having escaped from the Earth at time t_e (the associated location denoted by P_p) if the following two conditions are simultaneously satisfied [22],

$$H(t_e) > 0, \qquad r(t_e) > R_{\text{SOI}}, \tag{6}$$

where R_{SOI} is the radius of the sphere of influence (Table 1) and H is the Kepler energy of the spacecraft with respect to the Earth,

$$H(t) = \frac{v^2(t)}{2} - \frac{Gm_p}{r(t)}. \tag{7}$$

The function $H(t)$ is not constant due to the perturbation from the Moon and the Sun.

The capture set, i.e., the set of i.c.'s associated to ballistic capture orbits, is obtained by

$$\mathscr{C}^n_{-1} = \mathscr{X}_{-1} \cap \mathscr{W}_n. \tag{8}$$

Starting from the i.c. in $\mathscr{C}^n_{-1}$, a spacecraft can: 1) escape the Earth backwards in time ($\mathscr{X}_{-1}$), or equivalently approach it in forward time, and 2) perform at least n natural revolutions about the Earth ($\mathscr{W}_n$); refer to hyeraci2010 and luo2014a for details.

In general, the capture set $\mathscr{C}^n_{-1}$ will contain more than one point, while solutions with regular post-capture behaviors are more favorable as they can offer multiple repetitive insertion conditions. A stability index $\mathscr{S}$ has been introduced in luo2014a, that is

$$\mathscr{S} = \frac{t_n - t_0}{n}, \tag{9}$$

where t_n is the time at which the n-th revolution is accomplished. Physically speaking, the value of $\mathscr{S}$ depicts the mean orbital period in n revolutions [22, 31, 32].

3.2.3 Step 3: Low-thrust trajectory conversion

Each solution in the capture set corresponds to an escape point, P_p, which will be used as the patch point that connects the heliocentric trajectory and the ballistic capture part. Two-body Lambert algorithm is used for a second time to solve for the trajectory stretching from the asteroid to the patch point, P_p. The total delta-v is denoted by Δv_a.
All the candidates will be assessed in terms of fuel consumption and the post-capture stability, e.g., stability index $\mathscr{S}$ defined in [22], which is relevant to the risk assessment, such as the hazards associated to single-point injections or a broken-down component (see [24]). The output of the process is the best P_p, as well as its associated time, t_e.
Using the obtained impulsive Lambert arc as an initial guess, a method based on Pontryagin's maximum principle is adopted to convert it to a low-thrust trajectory; see, e.g., russell2007b, jiang2012, zhang2015. Since the low-thrust orbit design falls out of the scope of this work, only the optimization results will be given in Sec. 4.

3.3 Phase II: Aerobraking and LEO insertion

The objective of aerobraking is to diminish the energy of the spacecraft and, at the same time, to insure a given orbital inclination at the final LEO insertion. An initial maneuver is performed at the first periapsis (i.e., $P_{i.c.}$ at time t_0) in order to reduce the apoapsis altitude of the post-capture orbit, as shown in Figure.5. Thereafter, ABMs at the apoapsis, if necessary, will be executed to manage the parameters during atmospheric passages. Chemical impulses or a yawing angle of solar wings are introduced to nullify the inclination discrepancies, which form two aerobraking modes.

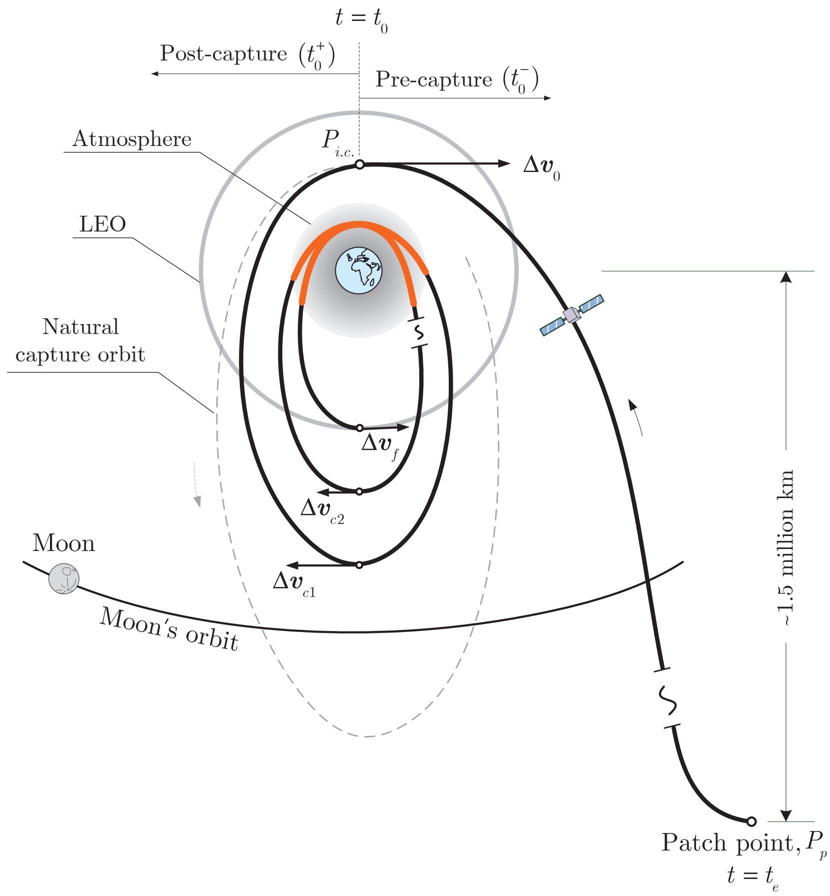

Figure 5 – Aerobraking and LEO insertion.

3.3.1 Mode 1: Inclination targeting by apoapsis maneuver

In the section, we present the difference of performing aerobraking during ballistic capture transfer with traditional aerobraking missions. As was done in the past Venus and Mars aerobraking missions, an insertion maneuver is used to capture the spacecraft into a highly elliptical orbit (e.g., apoapsis and periapsis altitude of $54,025.9$ km and 262.9 km for the Mars Global Surveyor), where the perturbing gravities can be nearly ignored [23]. In comparison, ballistic capture gently changes the Kepler energy and places the spacecraft on an elongated and weakly stable orbit by natural multi-body dynamics. To be specific, the post-capture apoapsis altitude reaches up to 1.5 SOI for the Sun-Mercury or Sun-Mars systems [41, 22]. As also noted in [22], the spacecraft can be deployed into a cislunar orbit after a close lunar swingby, although the approach condition is not trivial. Numerical experiments in the Earth-moon-sun system show that perturbing attractions will greatly increase the amount of ABMs, especially due to the Moon. For this reason, a periapsis maneuver Δv_0 at t_0 is suggested in order to brake the spacecraft into the near-Earth space. This operation is also beneficial to shorten the total capture time. This maneuver follows the inverse velocity vector. Thus, we have

$$\Delta v_0 = \sqrt{\frac{2}{r_0} - \frac{1}{0.5(r_0 + r_{a0})}} - v_0, \tag{10}$$

where r_{a0} is the required apoapsis distance after performing Δv_0. The updated mass is calculated by $m_1 = m_0 \exp \frac{-\Delta v_0}{c}$, where m_0 and m_1 are masses before and after the maneuver, respectively, and c is the exhaust velocity of the chemical propulsion system.

After Δv_0, a series of ABMs at apoapses are actualized to control the impact on solar panels, e.g., dynamic pressure in this paper. Throughout these ABMs, the maximum dynamic pressure is maintained within a safe range. Without loss of generality, a fixed maximum dynamic pressure is adopted, denoted by q_{max}. Special attention is paid to the orbital inclination with respect to the Earth because it involves the retrieval of the sample. Two strategies are developed and implemented for inclination management; the first one is based on chemical impulses, and the second one is based on the attitude control (i.e., maneuvers are no longer required).

According to the Gauss's equations, a maneuver vertical to the orbit plane is required to change the inclination for a small Δi

$$\Delta v_i = \Delta i \frac{na^2\sqrt{1-e^2}}{r\cos u} \tag{11}$$

where n, a, and e are the angular velocity, semi-major axis, and eccentricity, respectively, and $u = \omega + f$ is the argument of latitude (see Figure.**??**). For simplicity, the inclination maneuvers Δv_i are also implemented at apoapses, where the ABMs are performed. To minimize Δv_i of (11), a value of ω close to 0 or π is preferred. This echoes with the condition i) in Sect. **??**. Therefore, the total ABM at the k^{th} apoapsis is given by $\Delta v_{ck} = \sqrt{(\Delta v_{rk}^2 + \Delta v_{ik}^2)}$, where Δv_{rk} and Δv_{ik} are the in-plane and out-of-plane maneuvers at the k^{th} revolution, respectively. Note that Δv_{ik} is delimited by a maximum inclination correction, Δi_{max}. Appendix A derives the predicted aerobraking time from an initial apoapsis distance to a specified value by two-body assumptions (see Eq. (A12)).

3.3.2 Mode 2: Inclination targeting by aerodynamical force

A second method is proposed to economize on fuel. Recall the four configurations of solar wings in Figure.2. Case (c) and (d) will bring an out-of-plane aerodynamic force. As stated in Sect. 2.2 , only case (c) is considered for simplicity. Thus, the derivative of the inclination with respect to time is obtained by the Gauss's equations

$$\frac{\mathrm{d}i}{\mathrm{d}t} = \frac{\sqrt{1-e^2}\cos u}{na(1+e\cos f)} a_{an}, \tag{12}$$

where a_{an} is the drag component due to the yawing angle θ. Analytical equation (B4) in Appendix B show that the derivative of the inclination with respect to the time increases with the decrease of the semi-major axis. This reminds us that an efficient inclination correction strategy is to activate the yawing angle θ at the ending of aerobraking, where the semi-major axis is minimum. We assume solar wings are rotated to a non-zero θ at a semi-major axis a_θ and are fixed at θ until the required semi-major axis a_f is achieved. The in-plane and out-of-plane motions are coupled by the value of the yawing angle θ. The best situation is that the aerobraking terminates at a_f; meanwhile, the inclination arrives the required value, say, i_f (see Eqs. (B8) and (B9)). According to (B10), the value of a_θ varies with the yawing angle θ if i_θ is given. The flight time from i_θ to i_f is minimized using an optimization procedure (see from Eq. (B13) to Eq. (B16) in Appendix B).

The flowchart of constructing aero-ballistic capture orbits is summarized in Algorithm 1. Note that the first inclination correction strategy is activated until a critical apoapsis distance r_{a_i}, where perturbing attractions is negligible and the inclination is comparatively stable (see Sect. 4for more details).

Algorithm 1 Algorithm to derive aero-ballistic capture orbits.

```
θ = 0, k = 1
Set inclination control strategy (IncMode = 1 and 2 for chemical impulses and attitude controls, respectively
Calculate Δv_0 with (10), integrate (3) until next apoapsis, and obtain apoapsis distance r_ak
while r_ak > r_f do                                          ▷ r_f: apoapsis distance of the final orbit
    Compute orbital elements of k^th apoapsis, e.g., a_ak, e_ak, i_ak, and ω_ak
    if IncMode = 1 and r_ak < r_ai and |i_f − i_ak| > δi_f then   ▷ δi_f: allowable tolerance; see Sect. 4.
        if |i_f − i_ak| > Δi_max then
            Δi_k = sign(i_f − i_ak) · Δi_max
        else
            Δi_k = i_f − i_ak
        end if
        Compute Δv_ik with (11), where u_ak = ω_ak + π                                    ▷ f_ak = π
    else
        Δv_ik = 0
    end if
    if IncMode = 2 and r_ak < 0.1 SOI then                    ▷ 0.1 SOI is chosen by empirical analyses
        Calculate an optimization θ̄ and its corresponding semi-major axis a_θ̄
        if a_ak < a_θ̄ then
            Update the yawing angle θ with θ̄
            Set IncMode = 0                           ▷ close the optimization algorithm from now on
        end if
    end if
    Target required q_max for next atmospheric passage with a ABM Δv_rk
    Update the apoapsis velocity with Δv_ck, where Δv_ck = Δv_ik + Δv_rk
    Update the mass after Δv_ck by Tsiolkovsky's rocket equation
    Integrate (3) until next apoapsis
    k = k + 1
end while
```

4. Simulations

A spacecraft with the following configurations is used in the simulation: 1) the initial mass $m_0 = 600$ kg (at the asteroid departure epoch); 2) the reference area $S = 25$ m^2 with cases (a) and (c) of Figure.2; 3) the drag coefficient $C_{d0} = 1.95$; 4) a suit of impulse engines with $I_{\text{sp}} = 300$ s and $T_{\text{max}} = 240$ N and a suit of low-thrust engines with $I_{\text{sp}} = 3,000$ s and $T_{\text{max}} = 0.3$ N are equipped for trajectory correction maneuvers and interplanetary transfers, respectively.

The spacecraft is assumed to return samples from the asteroid 1991 VG, which has been proved as an easily retrievable object [11, 12]. The states of 1991 VG are obtained from the HORIZONS Interface of JPL Solar System Dynamics[2]; see Table 3. The parameters of other bodies involved are extracted from DE405 ephemeris. The Earth is considered as a standard sphere. The atmospheric exponential model is fitted from the 1976 U.S. Standard Atmosphere, i.e., $\rho_0 = 1.063 \times 10^{-8}$ kg/m^3, $h_0 = 125$ km, and $H = 6.78$ km [15]. These parameters are only available for a short altitude range near h_0. The atmosphere is deemed to rotate with the Earth. The maximum dynamic pressure is $q_{\text{max}} = 0.8$ N/m^2, which is slightly higher than the settings in [23, 24]. The critical apoapsis distance $r_{a_i} = 30\ R_e$ and $\Delta i_{\text{max}} = 1$ deg for each correction. The scenario that injects the spacecraft into the circular orbit of ISS is used and thus, $i_f = 51.6$ deg and $r_f \triangleq a_f = R_e + h_f$ ($\delta i_f = 0.05$ deg and $h_f = 360$ km).

Following the procedure of Sect. **??**, we can obtain the rough return epochs firstly, as shown in Figure.6. Only these two-impulse orbital transfers that can be converted to low-thrust trajectories are

[2] see http://ssd.jpl.nasa.gov/horizons.cgi/ [retrieved 12 January 2015].

Table 3 – Orbital elements of 1991 VG at JD 2457023.5 in the Earth Mean Equator and Equinox J2000.0 frame.

1991 VG	Semi-major axis, AU	Eccentricity	Inclination deg	RAAN deg	Pericenter anomaly, deg	Mean anomaly deg
Value	1.02696	4.91488E-02	2.38764E+01	3.43399E+00	9.53927E+01	3.95188E+01

presented (refer to Eq. (**??**)). The total maneuvers Δv_a to L_1 and L_2 points of the Sun-Earth system are illustrated by colored bars. Four epochs with local minimum maneuvers (t_{min}) are labeled in Figure.6, i.e., 0 and 180 days from JD 2458092.5 for approaching by L_1 and -46 and 181 days from JD 2458092.5 for approaching by L_2. The epoch JD 2458092.5 corresponds to 5 December 2017. Both Lagrangian points are placed at a fixed distance of 1.5 million km from the Earth, in despite of the pulsating Sun-Earth distance.

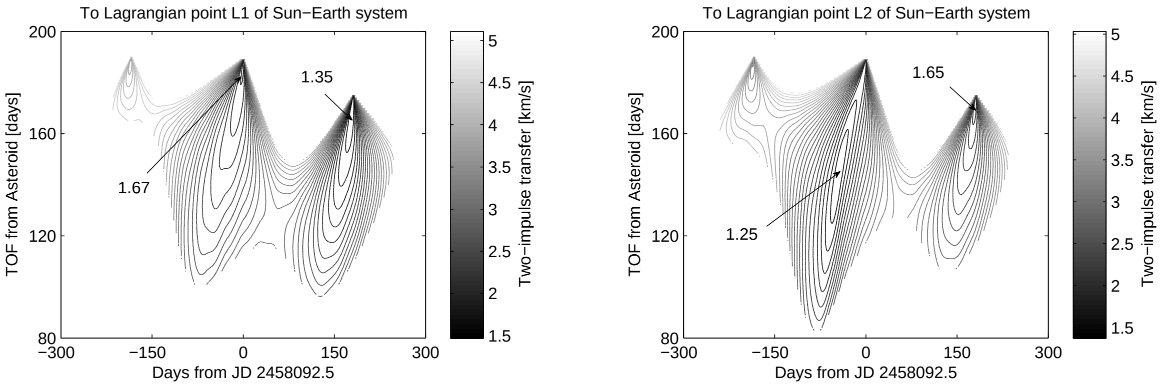

Figure 6 – Cost contours of two-impulse orbital transfer from 1991 VG to L_1 and L_2 of the Sun-Earth system (filtered by Eq. (**??**), where $c_t = 0.6$ and $m = m_0$). The horizontal axis represents the time that arrives L_1 or L_2.

Analyses show that the spacecraft will spend $1/8 \sim 1/4$ revolution period from the neighbourhood of Lagrangian points to the periapsis [39]. For this reason, the initial epoch t_0 for generating ballistic capture is $t_{\text{min}} \leq t_0 \leq t_{\text{min}} + T_e/4$, $\Delta t_0 = T_e/8$, where T_e is the period of the Earth around the Sun ($T_e = 365.25$ days). It is remarked that the Earth's atmosphere is used to decelerate the spacecraft. A small r_0 is essential so not to waste propellant for periapsis corrections. The parameters of initial conditions are: 1) the periapsis distance $r_0 \in [1R_e + \varepsilon, 1.2R_e]$ with spacing $\Delta r_0 = 10$ km, where $\varepsilon = 1$ km; 2) the osculating eccentricity $e_0 = 0.98$ and 0.99; 3) the inclination $i_0 = i_f$; 4) the RAAN Ω_0, $0 \leq \Omega_0 < 360$ deg, $\Delta\Omega_0 = 45$ deg; 5) the argument of periapsis ω_0, $0 \leq \omega_0 < 360$ deg, $\Delta\omega_0 = 0.5$ deg. The revolution number for the post-capture phase is $n = 6$, as was used in [41, 22]. This provides at least 5 more opportunities for orbit insertions, in case of any failure at t_0.
The transfer maneuvers from 1991 VG to the escape point P of each solution in $\mathscr{C}^6_{-1}$ is recalculated. As presented in Eq. (**??**), the index J_1 consists of two portions: Δv_l and Δv_c, where Δv_l relies on the value of Δv_a to the point P and Δv_c depends on Δv_0 and subsequent ABMs Δv_{c1}, Δv_{c2}, etc. The value of Δv_0 is determined by r_0, v_0, and r_{a0} according to Eq. (10), where r_0 and v_0 are relevant to the so-called "stability index $\mathscr{S}$" (a quantitative index that describes the post-capture stabilities; see [22] for details). Figure.7 shows a capture set $\mathscr{C}^6_{-1}$ with values of $t_0 = 2458092.5$ JD, $e_0 = 0.98$, and $\Omega_0 = 315$ deg. The value of Δv_a of each solution in $\mathscr{C}^6_{-1}$ is the minimum transfer maneuver from 1991 VG to its corresponding point P when the departure time varies. As noted in Figure.7, sample A has a minimum stability index, sample C has a minimum Δv_a, and sample B reaches a trade-off between stability index and Δv_a. Solutions A, B, and C are chosen as candidates of the aero-ballistic capture.
Table 4 shows fuel costs and final orbital parameters of the samples A to C with different insertion strategies. An impulsive strategy is presented for comparison and only the sample B is taken as an example due to their similarities. The spacecraft arrives a periapsis altitude of 181 km at t_0. An

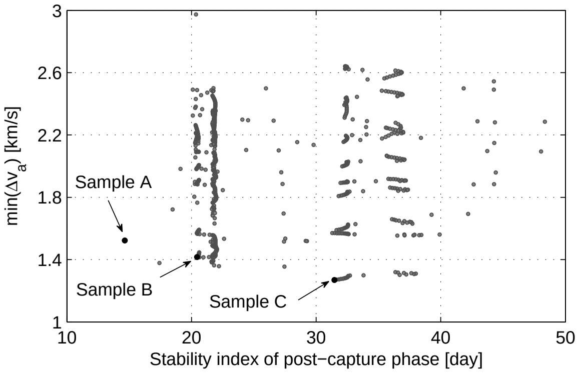

Figure 7 – Stability index vs. two-impulse transfer maneuvers to the switch point P.

initial maneuver Δv_l injects it into a transfer orbit of 181×360 km and then an apoapsis maneuver Δv_f achieves the final circular orbit (360×360 km and i_f). The capture time Δt_c is counted from t_0 to the epoch of Δv_f, i.e., a half period of the transfer orbit and Δt is the time from the asteroid departure to the epoch of Δv_f. Two inclination modes are presented in Table 4 and the capture maneuver $\Delta v_c = \Delta v_r + \Delta v_i + \Delta v_f$. Note that q_{max} of the final aerobraking revolution may be less than 0.8 N/m^2 for arriving an apoapsis altitude of 360 km. In Table 4, the solutions A and C has a maximum and minimum Δv_l, respectively; however, the solution B has a minimum total ABMs and thus has maximum residual masses for both modes. Also, the second inclination control strategy can save the fuel cost at the expense of the flight time; i.e., m_f/m_0 increases from 0.866 to 0.872 and the aerobraking time is elongated for 2 days, taking the sample B for instance. The final inclination meets the requirement. This also demonstrates the feasibility of the analytical derivations and approximations in Appendices A and B.

Table 4 – A comparison of different insertion strategies

Sample	Strategy	Maneuvers (m/s)				Flight time (days)		$\frac{m_f}{m_0}$	Science orbit	
		Δv_l	Δv_r	Δv_i	Δv_f	Δt	Δt_c		h_f, km	i_f, deg
B	Impulse	1,495.8	3,121	–	51.9	206.0	0.031	0.323	360	51.60
A		1,590.0	206.1	35.4	70.8	430.0	221.0	0.857		51.61
B	Mode-1	1,495.8	184.0	37.3	70.8	429.1	223.1	0.866	360	51.62
C		1,485.9	219.0	38.5	70.8	426.6	220.6	0.856		51.63
A		1,590.0	205.5	0	70.8	432.4	223.4	0.863		51.60
B	Mode-2	1,495.8	183.1	0	70.8	431.2	225.2	0.872	360	51.61
C		1,485.9	218.5	0	70.8	429.2	223.2	0.862		51.60

Figure.8(a) shows the trajectory from the asteroid departure to the epoch that 6 post-capture revolutions are accomplished (the sample B). The geocentric ballistic capture and ABC orbits are presented in Figure.8(b). The apoapsis distance of ABC orbit is greatly reduced due to Δv_0. This can be clearly recognized in Figure.8(d). The mass history is illustrated in Figure.8(c), where Δv_0 is larger than the subsequent ABMs.
More details are reported in Figure.9. The solar panels are rotated to an optimized yawing angle $\bar{\theta}$ for Mode-2 (see Figure.9(c)). Figure.9(d) shows that the variation of RAAN and argument of periapsis can be ignored (see Eq. (B5) and (B6) in Appendix B).
As previously mentioned, the value of Δv_0 depends on r_{a0}, e.g., an initial maneuver of 83 m/s inserts the spacecraft into an orbit with an apoapsis distance of 40 R_e (see Figure.9(a)). In principle, a lower r_{a0} is helpful to reduce third-body perturbations and to shorten the ABC duration; however, it requires a higher Δv_0 and more fuel consumption.

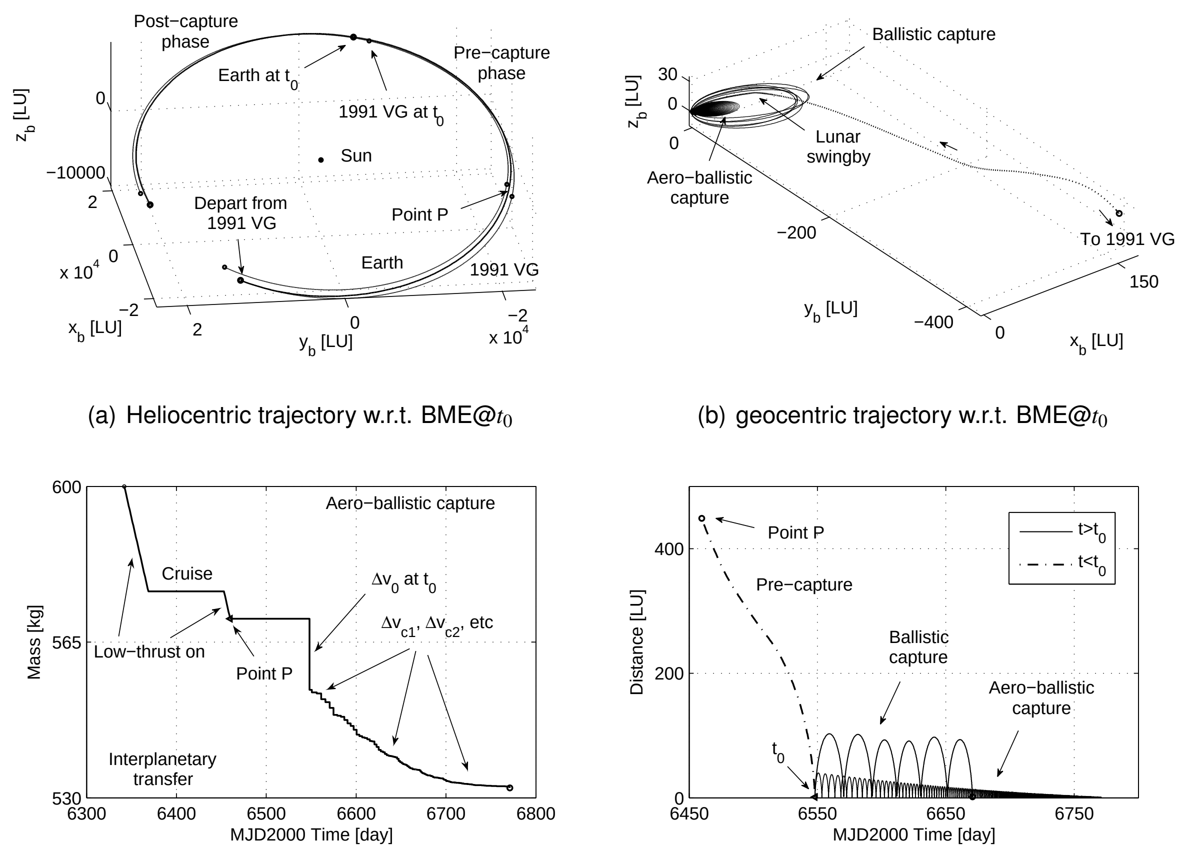

(a) Heliocentric trajectory w.r.t. BME@t_0 (b) geocentric trajectory w.r.t. BME@t_0

(c) Spacecraft's mass (d) Distance w.r.t. the Earth

Figure 8 – Trajectories, mass, and distance of the sample B in Figure.7.

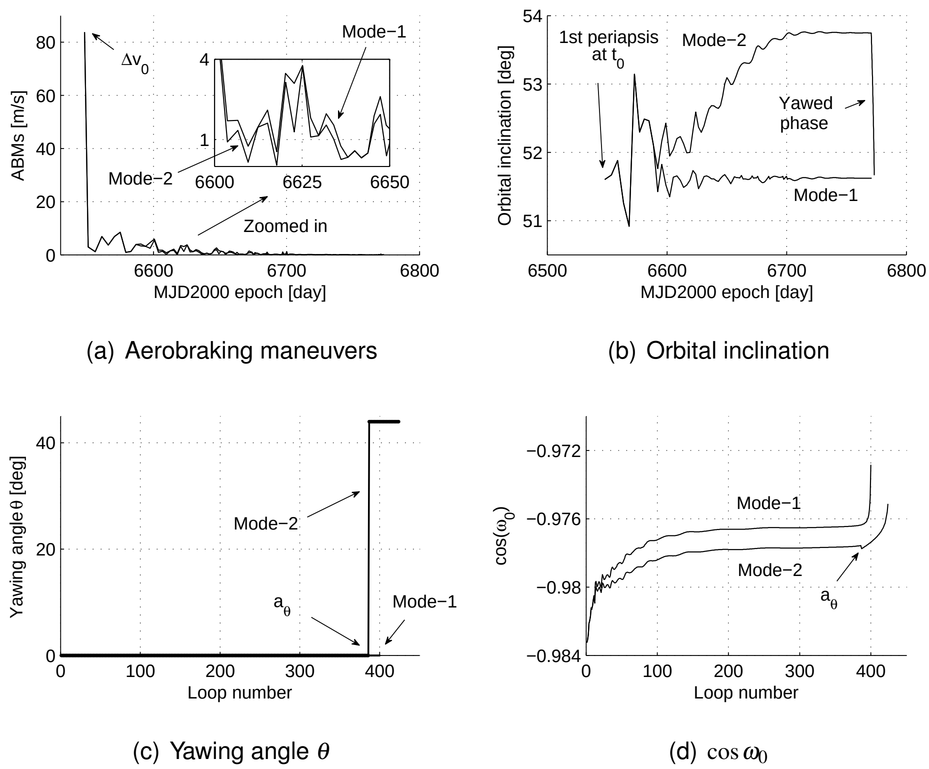

(a) Aerobraking maneuvers (b) Orbital inclination

(c) Yawing angle θ (d) $\cos \omega_0$

Figure 9 – Parameter profiles of the sample B during aero-ballistic capture.

5. Conclusions

This paper studies the method of constructing low-thrust, low-energy transfers from a near-Earth asteroid to a low-Earth orbit. The transfer consists of a heliocentric transfer and an aero-ballistic capture. The asteroid departure epoch is estimated by solving a two-body Lambert problem. Candidate ballistic capture orbits are obtained by an intersection manipulation. Preferable solutions are selected by several performance indices. Two inclination control strategies are introduced. Numerical simulations demonstrate the feasibility of the whole algorithm. The method proposed can be applied in the asteroid sample return or even asteroid retrieval missions.

6. Copyright Issues

The copyright statement is included in the template and must appear in your final pdf document in the position, style and font size shown below. If you do not include this in your paper, ICAS is not allowed and will not publish it.

7. Archiving

The ICAS 2024 proceedings will receive an ISBN number and will be cataloged, and archived by the German National Library.

8. Contact Author Email Address

Zongfu Luo: luozf@nju.edu.cn
Yijun Lian: lianyijun09@nudt.edu.cn
Chen Zhang: chenzhang@csu.ac.cn
Tao Zhang: zhangt358@mail.sysu.edu.cn

9. Copyright Statement

Acknowledgements

The authors acknowledge the financial support from the National Natural Science Foundation of China (No. 11602301, 11602297), the Science and Technology Laboratory on Space Intelligent Control for National Defense (No. KGJZDSYS-2018-12) and the National Key R&D Program of China (No. 2019YFA0706601).

Appendix A: Analytical Prediction of Aerobraking Time

The reduction of the semi-major axis a per periapsis passage can be found in [42]. It is briefly recalled for derivations in Appendix B. The derivative of a with respect to the time is formulated as follows according to the Gauss's equations

$$\frac{\mathrm{d}a}{\mathrm{d}t} = -\frac{2\sqrt{1+2e\cos f + e^2}}{n\sqrt{1-e^2}} a_a. \tag{A1}$$

The Earth's rotation and wing's yawing angle is not considered. Substituting the Kepler's equation and the Vis Viva equation into (A1), we obtain the derivative of a with respect to the eccentric anomaly E

$$\frac{\mathrm{d}a}{\mathrm{d}E} = -\rho A a^2 \left[\frac{(1+e\cos E)^3}{1-e\cos E}\right]^{\frac{1}{2}}, \tag{A2}$$

where $A = C_{d0}S/m$. Assume for simplicity that the reference altitude h_0 is exactly the altitude at pericenter and ρ_0 is the density at pericenter. Reusing the Kepler's equation, the exponential model is rearranged in terms of E as follows:

$$\rho = \rho_0 \exp\left[-\kappa(1-\cos E)\right], \tag{A3}$$

where $\kappa = ae/H$. Hence,

$$\frac{\mathrm{d}a}{\mathrm{d}E} = -\rho_0 A a^2 \exp\left[-\kappa(1-\cos E)\right]\left[\frac{(1+e\cos E)^3}{1-e\cos E}\right]^{\frac{1}{2}}. \tag{A4}$$

The fact that the aerobraking occurs in the vicinity of pericenter for an highly elliptic orbit. The eccentric anomaly E is a small quantity close to 0. Thus, we have

$$1-\cos E = 2\sin^2\frac{E}{2} \approx \frac{E^2}{2}. \tag{A5}$$

Integrating Eq. (A4) in combination with (A5), we obtain the semi-major axis variation over one revolution

$$\begin{aligned}\Delta a =& \int_0^{2\pi}\frac{\mathrm{d}a}{\mathrm{d}E}\mathrm{d}E \\ \approx& -\rho_0 A a^2 \int_0^{2\pi}\exp\left(-\kappa\frac{E^2}{2}\right)\left[\frac{(1+e\cos E)^3}{1-e\cos E}\right]^{\frac{1}{2}}\mathrm{d}E \\ \approx& -\rho_0 A a^2\left[\frac{(1+e)^3}{1-e}\right]^{\frac{1}{2}}\int_{-\infty}^{\infty}\exp\left(-\kappa\frac{E^2}{2}\right)\mathrm{d}E.\end{aligned} \tag{A6}$$

Since $\int_{-\infty}^{\infty}\exp(-x^2) = \sqrt{\pi}$ (Gaussian integral), then clearly,

$$\Delta a \approx -\rho_0 A a^2\left[\frac{(1+e)^3}{1-e}\right]^{\frac{1}{2}}\sqrt{\frac{2\pi}{\kappa}}. \tag{A7}$$

An equivalent conclusion was presented in [23, 43, 44]. Suppose now that we are interested in the secular prediction of semi-major axis. The average value of Δa over one orbit reads

$$\begin{aligned}\overline{\frac{\mathrm{d}a}{\mathrm{d}t}} =& \frac{\Delta a}{2\pi\sqrt{a^3/\mu_c}} \\ =& -\frac{\rho_0 C_{d0} S}{m}\left[\frac{\mu_c H(1+e)^3}{2\pi e(1-e)}\right]^{\frac{1}{2}}.\end{aligned} \tag{A8}$$

The pericenter density ρ_0 is, apparently, relevant to the maximum dynamic pressure P_{max}

$$\rho_0 = \frac{2q_{\mathrm{max}}}{v_p^2} = \frac{2q_{\mathrm{max}}}{\mu_c(\frac{2}{r_0}-\frac{1}{a})}. \tag{A9}$$

Thus,

$$\overline{\frac{\mathrm{d}a}{\mathrm{d}t}} = -\sqrt{\frac{2H}{\pi\mu_c}}\frac{q_{\mathrm{max}}C_{d0}S}{m}\left[\mathscr{G}(a)\right]^{-1}, \tag{A10}$$

where $\mathscr{G}(a)$ is a function of a, as

$$\mathscr{G}(a) = \sqrt{\frac{a-r_0}{ar_0(2a-r_0)}}. \tag{A11}$$

Simulations show that the periapsis distance varies slightly from a revolution to the next one, so that, r_0 is taken as a constant during aerobraking. Therefore, Eq. (A11) is a function that only depends on the value of a. Rearranging (A10) and integrating both sides, we obtain the aerobraking time from an initial a_i to a final a_f

$$\int_{a_0}^{a_f}\mathscr{G}(a)\mathrm{d}a = -\sqrt{\frac{2H}{\pi\mu_c}}\frac{q_{\mathrm{max}}C_{d0}S}{m}\Delta t. \tag{A12}$$

As no explicit integral for $\mathscr{G}(a)$ is found, numerical technology is used to solve (A12).

Appendix B: Optimization of Yawing Flight Time

When the yawing angle $\theta \neq 0$, the drag component along the orbital normal vector is written as

$$\begin{aligned} a_{an} =& a_a \cos^2\theta \sin\theta \\ =& \frac{c\mu_c \rho A(1+2e\cos f + e^2)}{2a(1-e^2)} \end{aligned} \tag{B1}$$

by using configuration (c) of Fig. 2, where $\theta = \alpha$ and $c = \cos^2\theta\sin\theta$. Following the manner of Appendix A, we have, from Eq. (12)

$$\begin{aligned} \frac{\mathrm{d}i}{\mathrm{d}E} =& \frac{\rho_0 caA\cos\omega(1+e\cos E)(\cos E - e)\exp\left[-\kappa(1-\cos E)\right]}{2\sqrt{1-e^2}} \\ &- \frac{\rho_0 caA\sin\omega\sin E(1+e\cos E)\exp\left[-\kappa(1-\cos E)\right]}{2}. \end{aligned} \tag{B2}$$

As $\sin E$ is an odd function, the integral of the second term in the right-side of (B2) is zero. As was done in (A6), the inclination change over one orbit is approximated by

$$\begin{aligned} \Delta i =& \int_0^{2\pi} \frac{\mathrm{d}i}{\mathrm{d}E}\mathrm{d}E \\ \approx& \rho_0 caA\cos\omega \int_0^{2\pi} \frac{(1+e\cos E)(\cos E - e)}{2\sqrt{1-e^2}} \exp\left(-\kappa\frac{E^2}{2}\right)\mathrm{d}E \\ \approx& \rho_0 caA\cos\omega\sqrt{1-e^2}\int_{-\infty}^{\infty}\exp\left(-\kappa\frac{E^2}{2}\right)\mathrm{d}E \\ =& \rho_0 caA\cos\omega\sqrt{1-e^2}\sqrt{\frac{\pi}{2\kappa}}. \end{aligned} \tag{B3}$$

The average value over one loop is of the form

$$\overline{\frac{\mathrm{d}i}{\mathrm{d}t}} = \frac{\rho_0 C_{d0} S\sin\theta\cos^2\theta\cos\omega}{am}\sqrt{\frac{\mu_c H(1-e^2)}{\pi e}}. \tag{B4}$$

Similarly, the derivatives of RAAN and argument of periapsis are obtained as

$$\overline{\frac{\mathrm{d}\Omega}{\mathrm{d}t}} = \frac{\rho_0 C_{d0} S\sin\theta\cos^2\theta\sin\omega}{am\sin i}\sqrt{\frac{\mu_c H(1-e^2)}{\pi e}} \tag{B5}$$

and

$$\overline{\frac{\mathrm{d}\omega}{\mathrm{d}t}} = -\cos i\overline{\frac{\mathrm{d}\Omega}{\mathrm{d}t}}. \tag{B6}$$

Obviously, the inclination can be decoupled from Ω and ω when $\omega = 0$ or π. In this case, $\overline{\frac{\mathrm{d}\Omega}{\mathrm{d}t}} = \overline{\frac{\mathrm{d}\omega}{\mathrm{d}t}} = 0$. Besides, $\overline{\frac{\mathrm{d}\omega}{\mathrm{d}t}} = 0$ when $i = \pi/2$. The derivative of a is directly written by multiplying (A8) with $\cos^3\theta$, as

$$\overline{\frac{\mathrm{d}a}{\mathrm{d}t}} = -\frac{\rho_0 C_{d0} S\cos^3\theta}{m}\left[\frac{\mu_c H(1+e)^3}{2\pi e(1-e)}\right]^{\frac{1}{2}}. \tag{B7}$$

Note that $\overline{\frac{\mathrm{d}a}{\mathrm{d}t}}$ cubically decreases with the increase of θ, but is almost stable for a fixed θ during aerobraking, no matter $\theta = 0$ or $\theta \neq 0$.

The goal now is to calculate the semi-major axis a_θ, where the solar wings begin to be yawed to θ. The inclination associated with a_θ is i_θ. Dividing Eq. (B4) by Eq. (B7) and rearranging it, we have

$$\overline{\mathrm{d}i} = -\frac{\tan\theta\cos\omega(1-e)}{2a(1+e)}\overline{\mathrm{d}a}. \tag{B8}$$

Integrating both sides of (B8) and substituting $r_0 = a(1-e)$, we derive

$$\int_{i_\theta}^{i_f}\overline{\mathrm{d}i} = -\frac{r_0\tan\theta\cos\omega}{2}\int_{a_\theta}^{a_f}\frac{1}{2a^2 - r_0 a}\overline{\mathrm{d}a}, \tag{B9}$$

wherein ω and r_p is considered as constants. Solving the integrals in (B9), we have

$$i_f - i_\theta = \tan\theta\cos\omega\left[\tanh^{-1}\left(\frac{4a_f}{r_0}-1\right)-\tanh^{-1}\left(\frac{4a_\theta}{r_0}-1\right)\right]. \tag{B10}$$

Based on Eq. (B10), infinite values of a_θ and their corresponding θ can be found for a specific $\Delta i \triangleq i_f - i_\theta$. The yawing angle that requires a minimum flight time is exactly the solution expected, say, $\bar{\theta}$. For ease of notation, we will denote

$$\sigma = -\sqrt{\frac{2H}{\pi\mu_c}}\frac{q_{\text{max}}C_{d0}S}{m} \tag{B11}$$

and

$$\mathscr{F}(a_\theta) = \tanh^{-1}\left(\frac{4a_f}{r_0}-1\right)-\tanh^{-1}\left(\frac{4a_\theta}{r_0}-1\right). \tag{B12}$$

Referring to Eq. (A12), we can derive the aerobraking time when a yawing angle is imposed, as

$$\Delta t = \frac{\int_{a_\theta}^{a_f}\mathscr{G}(a)\mathrm{d}a}{\sigma\cos^3\theta}. \tag{B13}$$

Thus, the derivative of Δt with respect to a_θ is obtained by the chain rule

$$\begin{aligned}\frac{\mathrm{d}\Delta t}{\mathrm{d}a_\theta} &= \frac{3\sin\theta\int_{a_\theta}^{a_f}\mathscr{G}(a)\mathrm{d}a}{\sigma\cos^4\theta}\frac{\mathrm{d}\theta}{\mathrm{d}a_\theta} - \frac{\mathscr{G}(a_\theta)}{\sigma\cos^3\theta}\\ &= \frac{1}{\sigma\cos^3\theta}\underbrace{\left[3\tan\theta\int_{a_\theta}^{a_f}\mathscr{G}(a)\mathrm{d}a\frac{\mathrm{d}\theta}{\mathrm{d}a_\theta} - \mathscr{G}(a_\theta)\right]}_{\mathscr{L}(a_\theta)},\end{aligned} \tag{B14}$$

where $\frac{\mathrm{d}\theta}{\mathrm{d}a_\theta}$ is calculated from (B10)

$$\frac{\mathrm{d}\theta}{\mathrm{d}a_\theta} = -\frac{4\Delta i\cos\omega}{r_0\left[\Delta i^2 + \mathscr{F}^2(a_\theta)\cos^2\omega\right]\left[\left(\frac{4a_\theta}{r_0}-1\right)^2-1\right]}. \tag{B15}$$

Since $|\theta| < \pi/2$ and $\sigma \neq 0$, the flight time arrives its extremum (i.e., minimum) when and only when $\mathscr{L}(a_\theta) = 0$. Substituting (B15) into $\mathscr{L}(a_\theta) = 0$, we have

$$\begin{aligned}\mathscr{L}(a_\theta) =& -\frac{12\Delta i^2\int_{a_\theta}^{a_f}\mathscr{G}(a)\mathrm{d}a}{r_0\mathscr{F}(a_\theta)\left[\Delta i^2 + \mathscr{F}^2(a_\theta)\cos^2\omega\right]\left[\left(\frac{4a_\theta}{r_0}-1\right)^2-1\right]} - \mathscr{G}(a_\theta)\\ =&0.\end{aligned} \tag{B16}$$

As previously stated, no explicit integral is obtained for $\mathscr{G}(a)$. Again, numerical methods, e.g., the Newton's iteration, are used to solve a $a_{\bar{\theta}}$ that let $\mathscr{L}(a_{\bar{\theta}}) = 0$ and Δt be minimum.

References

[1] G. Mikael, V. Jeremie, and J. Robert. The population of natural Earth satellites. Icarus, 218(1):262 – 277, 2012.

[2] J.P. Sanchez and C.R. McInnes. Assessment on the feasibility of future shepherding of asteroid resources. Acta Astronautica, 73:49 – 66, 2012.

[3] B. Viorel, editor. Asteroids, Prospective Energy and Material Resources. Springer Berlin Heidelberg, 2013.

[4] T. Simon, M. Patrick, and J. S. Daniel. Deployment of a lander on the binary asteroid (175706) 1996 FG3, potential target of the european MarcoPolo-R sample return mission. Acta Astronautica, 89:60 – 70, 2013.

[5] W. Sam and W. Bong. Low-thrust trajectory optimization for asteroid exploration, redirect, and deflection missions. In 24th AAS/AIAA Space Flight Mechanics Meeting, Santa Fe, New Mexico, 26–30 January, pages 1–16, 2014.

[6] F. B. William, V. David, J. W. Kevin, D. Marco, M. Patrick, S. L. Dante, C. Humberto, C. C. Harold, J. Daniel, and R. Steven. In search of the source of asteroid (101955) Bennu: Applications of the stochastic YORP model. Icarus, 247:191 – 217, 2015.

[7] P. Michel, M.A. Barucci, A.F. Cheng, H. Bohnhardt, J.R. Brucato, E. Dotto, P. Ehrenfreund, I.A. Franchi, S.F. Green, L.-M. Lara, B. Marty, D. Koschny, and D. Agnolon. MarcoPolo-R: Near-Earth Asteroid sample return mission selected for the assessment study phase of the ESA program cosmic vision. Acta Astronautica, 93:530 – 538, 2014.

[8] B. John, C. Fred, F. Louis, and et. al. Asteroid Retrieval Feasibility Study. Technical report, Keck Institute for Space Studies, California Institute of Technology, Pasadena, California, 2012.

[9] H. Baoyin, Y. Chen, and J. F. Li. Capturing near earth objects. Research in Astronomy and Astrophysics, 10(6):587 – 598, 2010.

[10] H. Zaki, A. Christopher, and D. R. Shane. Capturing near-Earth asteroids around Earth. Acta Astronautica, 81(2):523 – 531, 2012.

[11] D. García Yárnoz, J.P. Sanchez, and C.R. McInnes. Easily retrievable objects among the NEO population. Celestial Mechanics and Dynamical Astronomy, 116(4):367–388, 2013.

[12] L. Neus, R. Yuan, J. M. Josep, and G. Gerard. Capturing small asteroids into a Sun-Earth Lagrangian point. Acta Astronautica, 95:176 – 188, 2014.

[13] H. Urrutxua, D. Scheeres, C. Bombardelli, J.L. Gonzalo, and J. Pelaez. What does it take to capture an asteroid? A case study on capturing asteroid 2006 RH120. In 24th AAS/AIAA Space Flight Mechanics Meeting, Santa Fe, New Mexico, 26–30 January, pages 1–20, 2014.

[14] E. V. Patricia and R. M. Colin. Low-Energy Capture of Asteroids onto Kolmogorov-Arnold-Moser Tori. Journal of Guidance, Control and Dynamics, 38(2):330 – 334, 2015.

[15] J. J. Bertin. Hypersonic Aerothermodynamics. AIAA, Washington, DC, 1994.

[16] C. Circi and P. Teofilatto. On the Dynamics of Weak Stability Boundary Lunar Transfers. Celestial Mechanics and Dynamical Astronomy, 79(1):41–72, 2001.

[17] B. Edward. Capture Dynamics and Chaotic Motions in Celestial Mechanics. Princeton University Press, Princeton, 2004.

[18] K. Yagasaki. Sun-Perturbed Earth-to-Moon Transfers with Low Energy and Moderate Flight Time. Celestial Mechanics and Dynamical Astronomy, 90:197–212, 2004.

[19] F. García and G. Gómez. A Note on Weak Stability Boundaries. Celestial Mechanics and Dynamical Astronomy, 97(2):87–100, 2007.

[20] D. Romagnoli and C. Circi. Earth–Moon Weak Stability Boundaries in the Restricted Three and Four Body Problem. Celestial Mechanics and Dynamical Astronomy, 103(1):79–103, 2009.

[21] F. Topputo and E. Belbruno. Computation of Weak Stability Boundaries: Sun–Jupiter System. Celestial Mechanics and Dynamical Astronomy, 105(1–3):3–17, November 2009.

[22] Z.-F. Luo, F. Topputo, F. Bernelli-Zazzera, and G.-J. Tang. Constructing ballistic capture orbits in the real Solar System model. Celestial Mechanics and Dynamical Astronomy, 120(4):433–450, 2014.

[23] P. Esposito, V. Alwar, S. Demcak, E. Graat, M. Johnston, and R. Mase. Mars Global Ssuveyor Navigation and Aerobraking at Mars. Greenbelt, MD, 1998. 13th International Conf. on Space Flight Dynamics, American Astronautical Society Paper 98-384.

[24] D. T. Lyons, J. G. Beerer, P. Esposito, and M. D. Johnston. Mars Global Surveyor: Aerobraking Mission Overview. Journal of Spacecraft and Rockets, 36(3):307–313, 1999.

[25] P. V. Tartabini, M. M. Munk, and R. W. Powell. Development and Evaluation of an Operational Aerobraking Strategy for Mars Odyssey. Journal of Spacecraft and Rockets, 42(3):423–434, 2005.

[26] J. C. Smith and J. L. Bell. 2001 Mars Odyssey Aerobraking. Journal of Spacecraft and Rockets, 42(3):406–415, 2005.

[27] A. S. David and T. Robert. Aerobraking Cost and Risk Decisions. Journal of Spacecraft and Rockets, 44(6):1285–1293, 2007.

[28] C. David, O. Daniel, S. Thomas, K. James, P. Jill, and P. Richard. Autonomous aerobraking for low-cost interplanetary missions. Acta Astronautica, 93:467 – 474, 2014.

[29] C. Circi. Properties of Transit Trajectory in the Restricted Three and Four-Body Problem. Advances in Space Research, 49(10):1506–1519, 2012.

[30] A. Carbone, M. Cinelli, C. Circi, and E. Ortore. Observing Mercury by a quasi-propellantless mission. Celestial Mechanics and Dynamical Astronomy, 132(8):1–14, 2020.

[31] Z.-F. Luo and F. Topputo. Analysis of Ballistic Capture in Sun-Planet Models. Advances in Space Research, 56(6):1030–1041, 2015.

[32] Z.-F. Luo and F. Topputo. Capability of Satellite-aided Ballistic Capture. Communications in Nonlinear Science and Numerical Simulation, 48:211–223, 2017.

[33] Z.-F. Luo. The Role of the Mass Ratio in Ballistic Capture. Monthly Notices of the Royal Astronomical Society, Accepted, 2020.

[34] G. W. Hughe, M. Macdonald, C. R. McInnes, A. Atzei, and P. Falkner. Sample Return from Mercury and Other Terrestrial Planets Using Solar Sail Propulsion. Journal of Spacecraft and Rockets, 43(4):828 – 835, 2006.

[35] X. Zeng, S. Gong, and J. Li. Fast solar sail rendezvous mission to near Earth asteroids. Acta Astronautica, 105(1):40 – 56, 2014.

[36] V. Szebehely. Theory of Orbits: The Restricted Problem of Three Bodies. Academic Press Inc., 1967.

[37] T. Yuichi, Y. Makoto, A. Masanao, M. Hiroyuki, and N. Satoru. System design of the Hayabusa 2–Asteroid sample return mission to 1999 JU3. Acta Astronautica, 91:356 – 362, 2013.

[38] W. Johnson, J. M. Longuski, and D. T. Lyons. Nondimensional Analysis of Reaction-Wheel Control for Aerobraking. Journal of Guidance, Control and Dynamics, 26(6):861–868, 2003.

[39] C. Circi and P. Teofilatto. Effect of Planetary Eccentricity on Ballistic Capture in the Solar System. Celestial Mechanics and Dynamical Astronomy, 93(1-4):69–86, 2005.

[40] N. Hyeraci and F. Topputo. The Role of True Anomaly in Ballistic Capture. Celestial Mechanics and Dynamical Astronomy, 116(2):175–193, 2013.

[41] N. Hyeraci and F. Topputo. Method to Design Ballistic Capture in the Elliptic Restricted Three-Body Problem. Journal of Guidance, Control, and Dynamics, 33(6):1814–1823, 2010.

[42] T. Sterne. An Introduction to Celestial Mechanics. Interscience Publishers Inc., New York, 1960.

[43] A. E. Roy. Orbital Motion. CRC Press, Boca Raton, 2004.

[44] C. Zhou and L. Liu. Time Needed to Use Aerobraking to Insert Planetary Low Orbiters. Journal of Spacecraft TT&C Technology, 32(5):438–443, 2013. (in Chinese).